On a Ghost Artifact in Ultra Low Field Magnetic Resonance Relaxation Imaging

P. Volegov, L. Schultz, M. Espy

Physics Division, Los Alamos National Laboratory, Los Alamos NM, USA 87545
e-mail: volegov@lanl.gov

***Abstract* – Nuclear magnetic resonance (NMR) and magnetic resonance imaging (MRI) are widely used techniques across numerous disciplines. While typically implemented at fields > 1 T, there has been continuous interest in the methods at much lower fields for reasons of cost, material contrast, or application. There have been numerous demonstrations of MR at much lower fields (from 1 μT to 1 mT), the so-called ultra-low field (ULF) regime. Approaches to ULF MR have included superconducting quantum interference device (SQUID) sensor technology for ultra-sensitive detection and the use of pulsed pre-polarizing fields to enhance the signal strength. There are many advantages to working in the ULF regime. However, due to the low strength of the measurement field, acquisition of MRI at ULF is more susceptible to ambient fields that cause image distortions. Imaging artifacts can be caused by transients associated with non-ideal field switching and from remnant fields in magnetic shielding, among other causes. In this paper, we introduce a general theoretical framework that describes effects of non-ideal measurement field inversion/rotation due to presence of these transient fields. We illustrate imaging artifacts via simulated and experimental examples.**

***Keywords* – Nuclear magnetic resonance, magnetic resonance imaging (MRI), ultra-low-magnetic-field (ULF), SQUID, sensor, pulsed pre-polarizing field, MRI imaging, imaging artifact, switching transient, remnant field, magnetic shielding**

I. INTRODUCTION

Nuclear magnetic resonance (NMR) and magnetic resonance imaging (MRI) are widely used techniques across numerous disciplines. NMR provides powerful probes of local and macromolecular chemical structure and dynamics. Due to utilization of magnetically shielded enclosures, pre-polarizing magnetic fields and improvements in superconducting quantum interference device (SQUID) sensor technology allowing ultra-sensitive detection in a pulsed field environment, it has become possible and practical to perform MR at very low fields (from 1 μT to 1 mT), the so-called ultra-low field (ULF) regime [1], [2]. Despite a reduction in sample magnetization compared to conventional (> 1T) NMR/MRI, the ULF regime has a number of unique features that can be advantageously exploited: imaging in the presence of metal or even through a metal container [3], low susceptibility artifacts, and enhanced T_1 contrast [4], [5], [6]. In addition, ULF NMR/MRI with SQUIDs is compatible with simultaneous measurements of bio-magnetic signals, a capability conventional systems cannot offer [7], [8], [9], [10].

The disadvantage of reduced sample magnetization associated with low fields can somewhat be mitigated by pre-polarization and the use of sensitive detectors such as SQUIDs. However, one significant disadvantage of ULF MRI is that, due to the low measurement field, acquisition

of MRI at ULF is more susceptible to ambient fields that can result in image distortions. There are several sources of both static and dynamic ambient fields. A widely used technique to measure the NMR signal at ultra-low fields consists of polarizing the sample in a large field B_p ~100 mT, then switching off B_p in a time short compared to T_1 and observing the free induction decay (FID) of the magnetization of the sample at a low field B_m. Switching off B_p inevitably results in a transient field arising from currents proportional to the rate of change of the magnetic field dB/dt induced in any conductive materials (e.g. other components of the experimental apparatus and surrounding equipment). Typically ULF NMR/MRI experiments are conducted inside an electro magnetically shielded enclosure that consists of several layers of mu-metal and/or aluminum. The residual magnetization of the high permeability layers results in static residual field. Transient fields are produced from eddy currents in the high conductivity layers due to the polarization field ramp down.

Effects of a static inhomogeneous residual field (a remanence field) and the technique for correction of such artifacts are analyzed in [11]. Here in this work we consider effects associated with a spatially homogeneous but time dependent transient residual field arising due to switching of direction of the measurement field. This residual field prevents us from ever achieving a true non-adiabatic (or adiabatic) condition of the inversion of the measurement field. As we shall show, it is failure to attain a true non-adiabatic condition that introduces the ghost artifact we consider here. In this paper, we introduce the general theoretical framework that describes effects of non-ideal measurement field inversion/rotation in the context of a gradient echo MRI protocol and illustrate associated imaging artifacts via simulated and experimental examples.

II. THEORY

A. Background

A gradient echo pulse sequence is one of the simplest pulse sequences used in ULF MRI. An example of such a sequence - 3D Fourier multiple gradient echo imaging - is shown in Fig. 1. The sequence consists of pre-polarization (B_p), phase encoding (G_y and G_z), and several echo intervals created by inverting both the measurement field (B_m) and the readout gradient (G_x). Typically the measurement field is inverted in order to compensate for the effects of its non-uniformity. During each echo interval, one complete line of Cartesian k-space is acquired. The images are obtained for each echo. The echo images can be analyzed together or separately to obtain $T_2^*(\mathbf{r})$ maps.

In the pulse sequence described here the polarization (B_p) and the measurement (B_m) fields are orthogonal.

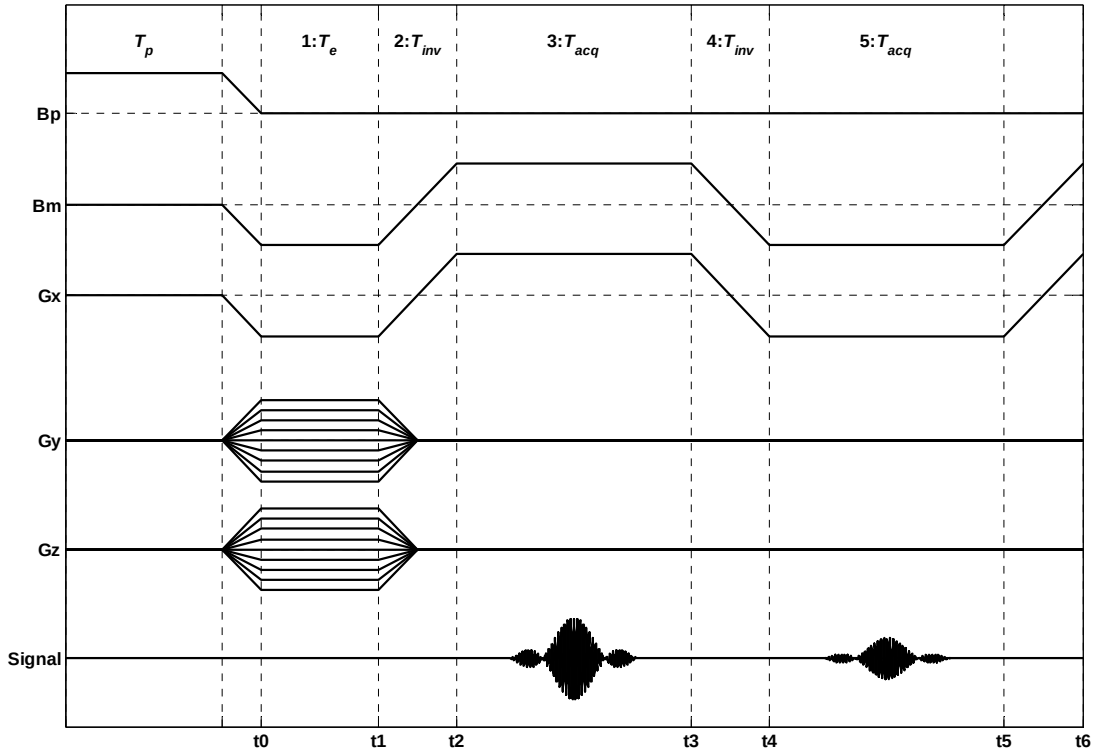

Fig. 1. Gradient echo imaging sequence. Here $\boldsymbol{T_p}$, $\boldsymbol{T_e}$, $\boldsymbol{T_{inv}}$, and $\boldsymbol{T_{acq} = 2T_e}$ denote duration of the corresponding time interval.

At several points during the pulse sequence fields are switched. For example B_p is removed after polarization and B_m is inverted between echoes. In the ideal case wherein the fields are switched non-adiabatically (i.e. the angular velocity of magnetic field rotation is much higher than the Larmor frequency), the magnetization remains aligned and precession of the bulk magnetization is directly observable without additional spin tipping RF pulses [12]. However, in addition to the measurement field and the gradients presented during the phase encoding and echo intervals, a residual field B_r arising from transients, or residual magnetization of the shielded room, is also present. This residual field prevents us from attaining a true non-adiabatic condition.

B. General Theory

To understand the consequences of not attaining a non-adiabatic condition we will consider solutions of the Bloch equation for the Fourier multiple gradient echoes imaging sequence.
Neglecting relaxation, the evolution of the nuclear magnetization **m** in the presence of a magnetic field **B** is described by the Bloch equation, which we will write in matrix notation [13]:

$$\frac{d\mathbf{m}}{dt} + \mathbf{\Omega}^{\times} \cdot \mathbf{m} = 0. \quad (1)$$

Here the matrix $\mathbf{\Omega}^{\times}$, called a rotation generator matrix, defines the rotation about vector $\mathbf{\Omega} \equiv \gamma \mathbf{B}$:

$$\mathbf{\Omega}^{\times} \equiv \begin{bmatrix} 0 & -\gamma B_z & \gamma B_y \\ \gamma B_z & 0 & -\gamma B_x \\ -\gamma B_y & \gamma B_x & 0 \end{bmatrix}, \quad (2)$$

where γ is gyromagnetic ratio, and the subscripts (x, y, z) refer to the Cartesian components of the vector. The cross notation, which denotes a rotation generator matrix associated with a vector (in our case the matrix $\mathbf{\Omega}^{\times}$, pronounced "omega-cross", associated with the vector $\mathbf{\Omega}$), is inspired by the relation $\mathbf{\Omega}^{\times} \cdot \mathbf{a} \equiv [\mathbf{\Omega} \times \mathbf{a}]$ and attributed to Prof. W. Kahan of the University of California (Berkeley) [14]. It is important to note that a rotation generator matrix is skew symmetric and traceless, so $\mathbf{\Omega}^{\times} = -\widetilde{\mathbf{\Omega}}^{\times}$ (here and later the tilde sign denotes a transpose matrix) and $\mathrm{trace}\{\mathbf{\Omega}^{\times}\} = 0$.

The change with time of the magnetic field $\mathbf{B}(t)$ can be described quite generally by a rotation and a scaling:

$$\mathbf{B}(t) = \frac{\omega}{\gamma} \cdot \mathbf{R} \cdot \hat{\mathbf{b}}_0, \quad (3)$$

where $\omega \equiv \omega(t)$ is the instantaneous precession frequency, $\mathbf{R} \equiv \mathbf{R}(t)$ is a proper rotation matrix, i.e. rotation without a reflection, which has the following properties: $\widetilde{\mathbf{R}} = \mathbf{R}^{-1}$, $\det(\mathbf{R}) = 1$; assuming that $\mathbf{R}(t = 0)$ is an identity matrix, and $\hat{\mathbf{b}}_0$ is a unit vector parallel to $\mathbf{B}(t = 0)$.

It is convenient to consider equation (1) in the rotating frame of reference that continuously follows the rotation of the magnetic field. To obtain the equation for the magnetization vector in the rotating frame, $\mathbf{m}' \equiv \widetilde{\mathbf{R}}(t)\mathbf{m}$, we use the usual approach to change the frame of reference (see for example [15]). Expressing the derivative of the magnetization vector in the laboratory frame through the derivative of the magnetization vector in the rotating frame:

$$\mathbf{m} \equiv \mathbf{R}(t)\mathbf{m}' \Rightarrow \frac{\mathrm{d}}{\mathrm{d}t}\mathbf{m} = \frac{\mathrm{d}}{\mathrm{d}t}(\mathbf{R}(t)\mathbf{m}') = \frac{\mathrm{d}\mathbf{R}}{\mathrm{d}t}\mathbf{m}' + \mathbf{R}\frac{\mathrm{d}\mathbf{m}'}{\mathrm{d}t}. \quad (4)$$

Substituting this last equation into equation (1), and using the identity $\left(\mathbf{R} \cdot \hat{\mathbf{b}}_0\right)^{\times} \equiv \mathbf{R} \cdot \hat{\mathbf{b}}_0^{\times} \cdot \widetilde{\mathbf{R}}$ we get the following equation for the evolution of the magnetic moment in the rotating reference frame:

$$\frac{d\mathbf{m}'}{dt} + \left(\omega\hat{\mathbf{b}}_0^{\times} + \psi\hat{\mathbf{u}}^{\times}\right) \cdot \mathbf{m}' = 0, \quad (5)$$

where $\psi\hat{\mathbf{u}}^{\times} \equiv \widetilde{\mathbf{R}}d\mathbf{R}/dt$ constitutes a fictitious magnetic field in the rotating frame of reference, ψ is the instantaneous angular velocity of magnetic field rotation, and a unit vector $\hat{\mathbf{u}}$ is the instantaneous axis of magnetic field rotation. The solution of equation (5) can be written as:

$$\mathbf{m}'(t) = \mathbf{U}(t)\mathbf{m}'_0. \quad (6)$$

Here $\mathbf{m}'_0 \equiv \mathbf{m}'(t = 0)$ is a constant vector and matrix $\mathbf{U}(t)$ satisfies the following differential equation:

$$\frac{d}{dt}\mathbf{U}(t) + \mathbf{\Omega}_{eff}^{\times}\mathbf{U}(t) = 0, \mathbf{U}(t = 0) = \mathbf{I}, \quad (7)$$

where $\mathbf{\Omega}_{eff}^{\times} \equiv \omega\hat{\mathbf{b}}_0^{\times} + \psi\hat{\mathbf{u}}^{\times}$ constitutes the effective magnetic field in the rotating frame of reference. Because the matrix $\mathbf{\Omega}_{eff}^{\times}$ is skew-symmetric and traceless, the matrix $\mathbf{U}(t)$ is a proper rotation matrix [15].

In the particular case, relevant to this work, wherein the effective magnetic field depends on time in such a way that for any times t and t' the matrices $\mathbf{\Omega}^{\times}_{eff}(t)$ and $\mathbf{\Omega}^{\times}_{eff}(t')$ commute, i.e. $\mathbf{\Omega}^{\times}_{eff}(t)\,\mathbf{\Omega}^{\times}_{eff}(t') = \mathbf{\Omega}^{\times}_{eff}(t')\,\mathbf{\Omega}^{\times}_{eff}(t)$, the evolution matrix $\mathbf{U}(t)$ is:

$$\mathbf{U}(t) = e^{-\int_0^t \mathbf{\Omega}^{\times}_{eff}(t')dt'}. \tag{8}$$

This commutation requirement, which is equivalent to the requirement that for any times t and t' the cross-product of the effective magnetic fields is zero, i.e. $\mathbf{B}_{eff}(t) \times \mathbf{B}_{eff}(t') = 0$, simply means that the direction of the effective magnetic field is constant. In practice this means that the magnetic field congruent with this condition rotates about a fixed axis with an angular velocity proportional to the magnitude of the field, i.e. $\psi(t) = a|\mathbf{B}(t)|$, where a is a constant.

Here it is convenient to note that if the eigenvectors of a matrix constitute an orthonormal basis then a matrix exponent can be written as:

$$e^{\mathbf{A}} = \sum_k e^{\lambda_k}\mathbf{v}_k\tilde{\mathbf{v}}_k, \tag{9}$$

where $\{\mathbf{v}_k\}$ and $\{\lambda_k\}$ are eigenvectors and eigenvalues of the matrix $\mathbf{A}$, i.e. $\mathbf{A}\mathbf{v}_k = \lambda_k\mathbf{v}_k$, and $\tilde{\mathbf{v}}_i \cdot \mathbf{v}_j = \delta_{i,j}$.

Any skew-symmetric matrix $\mathbf{a}^{\times}$ of the third order (associated with a vector $\mathbf{a}$) has the following eigenvalues [16]: $\lambda_k = ika, (k = -1,0,1)$, $i = \sqrt{-1}$, $a = |\mathbf{a}|$. The eigenvectors $\{\mathbf{v}_k\}_{-1}^{1}$ are not uniquely defined - any complex multiples of these eigenvectors are also eigenvectors. One convenient way to select the eigenvectors of the matrix $\mathbf{a}^{\times}$ is:

$$\mathbf{v}_0 = \hat{\mathbf{a}} \equiv \mathbf{a}/|\mathbf{a}|, \mathbf{v}_{\pm 1} = (\hat{\mathbf{b}} \pm i\hat{\mathbf{c}})/\sqrt{2}, \tag{10}$$

where $\hat{\mathbf{b}}$ is any unit vector orthogonal to $\hat{\mathbf{a}}$, $\hat{\mathbf{c}} = -\hat{\mathbf{a}} \times \hat{\mathbf{b}}$, i.e. $\{\hat{\mathbf{a}}, \hat{\mathbf{b}}, \hat{\mathbf{c}}\}$ is a right handed set.

Transforming equation (6) into the laboratory frame of reference, we have:

$$\mathbf{m}(t) = \mathbf{R}(t)\mathbf{U}(t)\widetilde{\mathbf{R}}(0)\mathbf{m}_0. \tag{11}$$

Here it is important to highlight two limiting cases: a) an adiabatic transition, wherein the spin precession frequency is much higher than the angular velocity of magnetic field rotation, i.e. $|\omega| \gg |\psi|$, and b) a non-adiabatic transition, wherein the spin precession rate is much lower than the rate of magnetic field rotation, i.e. $|\omega| \ll |\psi|$. In these two cases, a) and b), we can safely neglect either the $\psi\hat{\mathbf{u}}^{\times}$ or the $\omega\hat{\mathbf{b}}_0^{\times}$ term of the effective magnetic field $\mathbf{\Omega}^{\times}_{eff}$, respectively, to solve equation (7).

In the first case – adiabatic – the direction of the magnetic field is constant in the rotating frame and the solution of equation (7) is:

$$\mathbf{U}(t) = e^{-\varphi(t)\hat{\mathbf{b}}_0^{\times}}, \tag{12}$$

where $\varphi(t) = \int_0^t \omega(t')dt'$, so that the resulting magnetization in the laboratory frame is equal to:

$$\mathbf{m}(t) = \mathbf{R}(t)e^{-\varphi(t)\hat{\mathbf{b}}_0^{\times}}\widetilde{\mathbf{R}}(0)\mathbf{m}_0. \tag{13}$$

In the second case – non-adiabatic – the solution of equation (7) is:

$$\mathbf{U}(t) = \widetilde{\mathbf{R}}(t)\mathbf{R}(0), \tag{14}$$

which simply means the magnetization in the laboratory frame is constant, i.e. $\mathbf{m}(t) = \mathbf{m}_0$, on the time scale $t \sim 1/\psi$.

In the intermediate case, which arises due to presence of transient magnetic fields, ψ is on the order of ω, so we need to account for the both the $\psi\hat{\mathbf{u}}^{\times}$ and the $\omega\hat{\mathbf{b}}_0^{\times}$ terms in the solution of equation (7). Further on we will consider examples of such intermediate cases, in which solution of the equation (7) can be expressed by equation (8).

C. Gradient Echo Sequence

Now we will apply this formalism to a gradient echo pulse sequence (see Fig. 1). We start by analyzing the sequence after polarization field ramp down to keep the formalism which follows as simple as possible. We note that non-idealities associated with B_p ramp down will only influence the initial magnetization $\mathbf{m}_0$ and do not impact the ghost artifact we are considering here. These effects can be analyzed separately (see for example [11]). The B_p ramp will also create a transient magnetic field present during the phase encoding and readout intervals. While not considered explicitly here, the effects of this transient field are included in the rotation matrix $\mathbf{R}(t)$ that describes the field inversion between echoes. Neglecting the effects of the concomitant gradients, which are considered in detail in [17], [18], and assuming that the measurement field B_m is aligned along *z*-axis, the fields during this field sequence are:

1. Phase encoding, $t_0 \le t < t_1$:

$$\mathbf{B}(\mathbf{r}) = -\frac{1}{\gamma}(\omega_0 + (\tilde{\mathbf{g}}_{ph} + s_r\tilde{\mathbf{g}}_r) \cdot \mathbf{r})\hat{\mathbf{e}}_z, \tag{15}$$

where $\omega_0 = \gamma B_m$ is Larmor frequency, $\mathbf{g}_{ph}$ and $\mathbf{g}_r$ are Larmor frequency gradients along the phase encoding and the frequency encoding directions, respectively, and $s_r = \pm 1$ is the sign of the readout gradient during phase encoding. We assume that the frequency encoding direction is orthogonal to the phase encoding directions, i.e. $\tilde{\mathbf{g}}_{ph} \cdot \mathbf{g}_r = 0$. Here we are neglecting residual fields because the primary field, i.e. the measurement field and the gradient, is large and constant during this interval. The duration of this interval is T_e.

2. Field inversion, $t_1 \le t < t_2$:

$$\mathbf{B}(t) = -\frac{\omega(t-t_1)}{\gamma}\mathbf{R}(t-t_1) \cdot \hat{\mathbf{e}}_z. \tag{16}$$

Here the instantaneous Larmor frequency $\omega(t)$ and the rotation matrix $\mathbf{R}(t)$ are such that $\omega(0) = \omega(T_{inv}) = \omega_0$, and $\mathbf{R}(0) = \mathbf{I}$, $\mathbf{R}(T_{inv}) = e^{\pi\hat{\mathbf{u}}^{\times}}$, where $e^{\pi\hat{\mathbf{u}}^{\times}}$ is a rotation by angle π about an axis within the *x*-*y* plane defined by unit vector $\hat{\mathbf{u}}$:

$$\hat{\mathbf{u}} = \cos(\alpha)\,\hat{\mathbf{e}}_x + \sin(\alpha)\,\hat{\mathbf{e}}_y. \tag{17}$$

Here α is angle between magnetic field rotation axis and *x*-axis. Note that the matrix $\mathbf{R}(t)$ incorporates the effects of the residual fields. The duration of this interval is T_{inv}.

3. First echo readout, $t_2 \le t < t_3$:

$$\mathbf{B}(\mathbf{r}) = \frac{1}{\gamma}(\omega_0 + \tilde{\mathbf{g}}_r \cdot \mathbf{r})\hat{\mathbf{e}}_z. \tag{18}$$

The duration of this interval is $T_{acq} = 2T_e$.

4. Field inversion, $t_3 \le t < t_4$:

$$\mathbf{B}(t) = \frac{\omega(t-t_3)}{\gamma}\mathbf{R}(t-t_3)\cdot\hat{\mathbf{e}}_z. \tag{19}$$

5. Second echo readout, $t_4 \le t < t_5$:

$$\mathbf{B}(\mathbf{r}) = -\frac{1}{\gamma}(\omega_0 + \tilde{\mathbf{g}}_r\cdot\mathbf{r})\hat{\mathbf{e}}_z. \tag{20}$$

6. …etc.

The evolution of the magnetization with time during the first echo is:

$$\mathbf{m}^{(1)}(\mathbf{r},t') = e^{-(\omega_0+\tilde{\mathbf{g}}_r\cdot\mathbf{r})t'\hat{\mathbf{e}}_z^{\times}}\cdot e^{\pi\hat{\mathbf{u}}^{\times}}\mathbf{U}_{-}\cdot e^{(\omega_0+(\tilde{\mathbf{g}}_{ph}+s_r\tilde{\mathbf{g}}_r)\cdot\mathbf{r})T_e\hat{\mathbf{e}}_z^{\times}}\cdot\mathbf{m}_0, \tag{21}$$

where $\mathbf{U}_{\pm}$ is the solution of equation (7) with matrix $\boldsymbol{\Omega}_{eff}^{\times} = \pm\omega(t)\hat{\mathbf{e}}_z - \tilde{\mathbf{R}}d\mathbf{R}/dt$ during the field inversion interval, and $t' \equiv t - t_2$ is the time during the first echo interval.

It is convenient to re-write equation (21) using eigenvectors of the rotation generator matrix $\hat{\mathbf{e}}_z^{\times}$:

$$\mathbf{m}^{(1)}(\mathbf{r},t') = \sum_{l'=-1}^{1}\sum_{l=-1}^{1} Q_{l',l}^{(-)}\cdot e^{-il'(\omega_0+\tilde{\mathbf{g}}_r\cdot\mathbf{r})t'}\cdot e^{il(\omega_0+(\tilde{\mathbf{g}}_{ph}+s_r\tilde{\mathbf{g}}_r)\cdot\mathbf{r})T_e}\cdot\mathbf{v}_{l'}\cdot(\tilde{\mathbf{v}}_l\cdot\mathbf{m}_0), \tag{22}$$

where the summation coefficients $Q_{l',l}^{(\pm)}$ are defined by the following equation:

$$Q_{l',l}^{(\pm)} = \tilde{\mathbf{v}}_{l'}\cdot e^{\pi\hat{\mathbf{u}}^{\times}}\cdot\mathbf{U}_{\pm}\cdot\mathbf{v}_l;\ \mathbf{v}_0 = \hat{\mathbf{e}}_z,\ \mathbf{v}_{\pm1} = (\hat{\mathbf{e}}_x \mp i\hat{\mathbf{e}}_y)/\sqrt{2}. \tag{23}$$

Introducing *k*-space coordinates [19] we can write equation (22) as:

$$\mathbf{m}^{(1)}(\mathbf{r},\mathbf{k}) = \sum_{l'=-1}^{1}\sum_{l=-1}^{1} Q_{l',l}^{(-)}\cdot e^{-il'\mathbf{k}_r\cdot(\mathbf{r}+\mathbf{r}_0)}\cdot e^{il(\varphi_e+(\mathbf{k}_{ph}+s_r\mathbf{k}_0)\cdot\mathbf{r})}\cdot\mathbf{v}_{l'}\cdot(\tilde{\mathbf{v}}_l\cdot\mathbf{m}_0). \tag{24}$$

Here $\mathbf{k} = \mathbf{k}_{ph} + \mathbf{k}_r - \mathbf{k}_0$, where $\mathbf{k}_{ph} = \tilde{\mathbf{g}}_{ph}T_e$ and $\mathbf{k}_r = \tilde{\mathbf{g}}_r t'$ are the phase encoding and frequency encoding *k*-space coordinates respectively, $\mathbf{k}_0 = \tilde{\mathbf{g}}_r T_e$ is the extent of the MRI data acquisition in *k*-space coordinates along the frequency encoding dimension, $\varphi_e = \omega_0 T_e$, and $\mathbf{r}_0 = \omega_0\mathbf{g}_r/|\mathbf{g}_r|^2$ is the absolute offset of a field of view along the frequency encoding dimension.

Integrating equation (24) over the sample volume, the MRI signal measured during the first echo of this sequence may be written as:

$$S^{(1)}(\mathbf{k}) = \sum_{l'=-1}^{1}\sum_{l=-1}^{1} Q_{l',l}^{(-)}e^{il\varphi_0}\int T_{l'}^{*}(\mathbf{k},\mathbf{r})E_l(\mathbf{k},\mathbf{r})M_{l',l}(\mathbf{r})d^3r. \tag{25}$$

Here $\varphi_0 = \varphi_e - s_r\mathbf{k}_0\mathbf{r}_0$, the spatial encoding functions $E_l(\mathbf{k},\mathbf{r})$ and $T_{l'}(\mathbf{k},\mathbf{r})$ are defined by:

$$E_l(\mathbf{k},\mathbf{r}) \equiv e^{il(\mathbf{k}_{ph}+s_r\mathbf{k}_0)\cdot(\mathbf{r}+\mathbf{r}_0)}, \tag{26}$$

and

$$T_{l'}(\mathbf{k},\mathbf{r}) \equiv e^{il'\mathbf{k}_r\cdot(\mathbf{r}+\mathbf{r}_0)}. \quad (27)$$

The offset of a field of view along the frequency encoding dimension $\mathbf{r}_0$ can be always set to zero by demodulating the measured signal. The spatial sensitivity map $M_{l',l}(\mathbf{r})$ of a MRI system is defined by the following equation:

$$M_{l',l}(\mathbf{r}) \equiv (\tilde{\mathbf{F}}(\mathbf{r})\cdot\mathbf{v}_{l'})(\tilde{\mathbf{v}}_l\cdot\mathbf{m}_0(\mathbf{r})), \quad (28)$$

where a vector function $\mathbf{F}(\mathbf{r})$, sometimes called "lead field," describes the response of a sensor to a unit magnetic dipole at the position $\mathbf{r}$. Specifically $F_x(\mathbf{r})$ is the magnetic field flux through the pick-up coil of a sensor generated by a unit magnetic dipole aligned along *x*-axis. Correspondingly $F_y(\mathbf{r})$ and $F_z(\mathbf{r})$ are the magnetic field flux due to dipoles aligned along *y*- and *z*-axis. Due to the reciprocity principle, $\mathbf{F}(\mathbf{r})$ is equal to the magnetic field at the position $\mathbf{r}$ generated by unit current in a sensor pick-up coil.

D. Comparison between Adiabatic and Non-adiabatic Field Switching

In the non-adiabatic case we have $\mathbf{U}_{\pm} = e^{-\pi\hat{\mathbf{u}}^{\times}}$, see equation (14), resulting in $Q^{\pm}_{l',l} = \delta_{l',l}$. Substituting this expression into equation (25) we will obtain the following equation for the detected MRI signal:

$$S(\mathbf{k}) = e^{-i\varphi_0}\int e^{i\left(-\mathbf{k}_{ph}+(\mathbf{k}_r-s_r\mathbf{k}_0)\right)\cdot\mathbf{r}} e^{i\theta_{-1,-1}(\mathbf{r})} I(\mathbf{r})d^3r + c.c., \quad (29)$$

where $I(\mathbf{r}) = \left|M_{-1,\pm1}(\mathbf{r})\right|$, and $\theta_{l',l}(\mathbf{r}) = \arg\left(\tilde{\mathbf{F}}(\mathbf{r})\cdot\mathbf{v}_{l'}\right) + \arg\left(\tilde{\mathbf{v}}_l\cdot\mathbf{m}_0(\mathbf{r})\right)$. Note that the function $I(\mathbf{r})$ is the module of the image we reconstruct by applying a Fourier transform to the measured MRI signal, and $\theta_{-1,-1}(\mathbf{r})$ is the phase map of the reconstructed image. In equation (29) and later *c.c.* denotes the complex conjugate of the preceding term.

In the adiabatic case we have $\mathbf{U}_{\pm} = e^{\mp\varphi_T\hat{\mathbf{e}}_z^{\times}}$, where $\varphi_T = \int_0^{T_{inv}}\omega(t)dt$ (see equation (12)). Direct evaluation of equation (23) using, for example, *Rodrigues' Identity*:

$$e^{\varphi\hat{\mathbf{u}}^{\times}} = \mathbf{I} + \sin(\varphi)\hat{\mathbf{u}}^{\times} + \left(1-\cos(\varphi)\right)(\hat{\mathbf{u}}^{\times})^2, \quad (30)$$

gives $Q^{(\pm)}_{l',l} = e^{i\phi}\delta_{l',-l}$, where $\phi = \mp l\varphi_T + \alpha(l'-l) + \pi\delta_{l',0}\delta_{0,l}$. Using this expression to simplify equation (25) we will obtain:

$$S(\mathbf{k}) = e^{i\varphi_1}\int e^{i\left(\mathbf{k}_{ph}+(\mathbf{k}_r+s_r\mathbf{k}_0)\right)\cdot\mathbf{r}} e^{i\theta_{-1,1}(\mathbf{r})} I(\mathbf{r})d^3r + c.c., \quad (31)$$

where $\varphi_1 = \varphi_0 + \varphi_T + 2\alpha$, and recall that α is angle between magnetic field rotation axis and x-axis, see equation (17).

Comparing these two expressions, i.e. non-adiabatic vs. adiabatic, we observe that the sign of the phase encoding dimensions is flipped relative to the readout dimension - compare $-\mathbf{k}_{ph}+\mathbf{k}_r$ in (29) vs. $+\mathbf{k}_{ph}+\mathbf{k}_r$ in (31). Moreover, in order to form an echo, the sign of the readout gradient during the phase encoding step should be different for adiabatic and non-adiabatic field inversion (compare $(\mathbf{k}_r - s_r\mathbf{k}_0)$ in (29) vs. $(\mathbf{k}_r + s_r\mathbf{k}_0)$ in (31)). Specifically, to form a gradient echo in the non-adiabatic case the gradient along the readout direction during the phase encoding step should be opposite to the gradient during the readout step, meaning we should select $+\tilde{\mathbf{g}}_r$, i.e. $s_r = +1$, in equation (15). In the case of an adiabatic field inversion these gradients should be

the same, so we should select $-\tilde{\mathbf{g}}_r$, i.e. $s_r = -1$ in (15). To paraphrase from the physical analogies presented in [12] the non-adiabatic field inversion forms "pancake" echoes in which precession direction does not change from the point of view associated with the magnetic field direction, but relative position between leading and lagging spins is "flipped." The adiabatic transition forms "race-track" echoes in which the precession spontaneously reverses with no change in relative position of spins. From eqs. (29) and (31) we see that the adiabatic and non-adiabatic cases each result in different, but artifact free, echo images that may be analyzed in a straightforward manner.

E. Intermediate Field Switching

In the intermediate case, when we cannot attain a true non-adiabatic or adiabatic condition, the expression for the MRI signal will contain both $e^{i(\mathbf{k}_r-\mathbf{k}_{ph})\cdot\mathbf{r}}$ and $e^{i(\mathbf{k}_r+\mathbf{k}_{ph})\cdot\mathbf{r}}$ terms, or a mixture of both "pancake" and "racetrack" echo behavior. We will show that this results in specific imaging artifacts that we will illustrate in detail.

Considering a "pancake" echo case, *i.e.*, a non-adiabatic field rotation with $s_r = +1$, and neglecting the overall shift along the frequency encoding dimension $\mathbf{r}_0$, which always can be removed by demodulating the MRI signal, we can explicitly write the detected MRI signal during the first echo interval:

$$S^{(1)}(\mathbf{k}) = \sum_{l=-1}^{1} S_l^{(1)}(\mathbf{k}) + c.c. = Q_{-1,-1}^{(-)} \int e^{i\left(-\mathbf{k}_{ph}+(\mathbf{k}_r-\mathbf{k}_0)\right)\cdot\mathbf{r}} e^{i\theta_{-1,-1}(\mathbf{r})} I(\mathbf{r}) d^3r + \\ + Q_{-1,1}^{(-)} \int e^{i\left(\mathbf{k}_{ph}+(\mathbf{k}_r+\mathbf{k}_0)\right)\cdot\mathbf{r}} e^{i\theta_{-1,1}(\mathbf{r})} I(\mathbf{r}) d^3r + Q_{-1,0}^{(-)} \int e^{i\mathbf{k}_r\cdot\mathbf{r}} I_r(\mathbf{r}) d^3r + c.c., \quad (32)$$

where $\mathbf{k} = -\mathbf{k}_{ph} + \mathbf{k}_r - \mathbf{k}_0$, and $I_r(\mathbf{r}) = \left|M_{-1,0}(\mathbf{r})\right|$.

It is convenient to visualize the terms $S_l^{(1)}(\mathbf{k})$ from equation (32) as *k*-space trajectories in order to understand physical meaning of these functions (see Fig. 2).

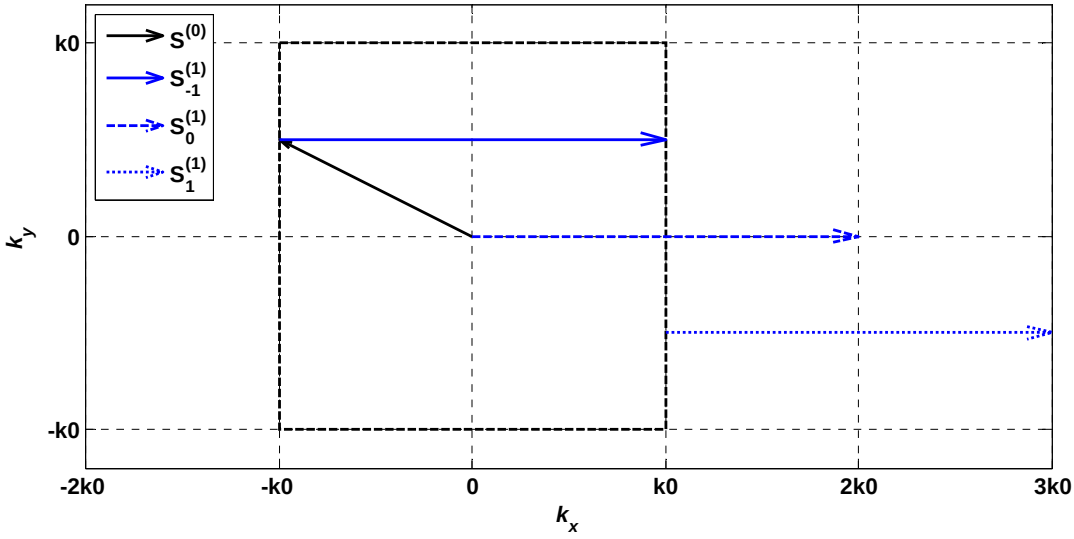

Fig. 2. *K*-space trajectories for the first echo. The dashed rectangle denotes the sampled area. The term $\boldsymbol{S}^{(0)}$ corresponds to the *k*-space trajectory during the phase encoding step. The term $\boldsymbol{S}_{-1}^{(1)}$ describes the trajectory in the case of ideal non-adiabatic field inversion. Terms $\boldsymbol{S}_{0}^{(1)}$ and $\boldsymbol{S}_{1}^{(1)}$ arise in the case of non-ideal field inversion.

The first term in the right hand side of this equation, denoted $S_{-1}^{(1)}(\mathbf{k})$, represents a properly encoded echo signal which will result in an artifact free image after applying a Fourier transform to equation (32).

The second term, denoted $S_{1}^{(1)}(\mathbf{k})$ due to offset $+\mathbf{k}_0$ does not form the echo signal and samples *k*-space outside the target area. Thus, if we select appropriately the extent of the sampled *k*-space to encompass the significant frequency content of the scene, an artifact image corresponding to this term is negligible. Note, however, that in this term phase encoded directions are inverted.

Finally, the third term in equation (32), $S_{0}^{(1)}(\mathbf{k})$, represents a FID like signal due to the fraction of magnetization aligned with the measurement field at the time point right after the polarizing field is switched off. If the polarization and the measurement fields are exactly orthogonal and the polarization is switched off ideally non-adiabatically, then this term is equal to zero. However, if initially the magnetization is not perfectly orthogonal to the measurement field or the ideal non-adiabatic condition is not achieved during polarization field ramp down, then this term results in an artifact, which manifests itself as a bright line along the frequency encoding dimension, because, as may be seen from equation (32), this fraction of the magnetization is not phase encoded. We will illustrate this artifact further below.

We can apply the same approach for steps 4 and 5 of the pulse sequence (see equations (19) and (20)) to obtain the detected MRI signal during the second echo:

$$S^{(2)}(\mathbf{k}) = \sum_{l'=-1}^{1} \sum_{l=-1}^{1} S_{l',l}^{(2)}(\mathbf{k}) + c.c. = \tag{33}$$

$$= \sum_{l'=-1}^{1} \sum_{l=-1}^{1} Q_{1,l'}^{(+)} Q_{l',l}^{(-)} e^{il\varphi_0} \int T_1(\mathbf{k}, \mathbf{r}) T_{l'}^{*}(2\mathbf{k}_0, \mathbf{r}) E_l(\mathbf{k}_1, \mathbf{r}) M_{1,l}(\mathbf{r}) d^3r + c.c.,$$

where $\mathbf{k}_1 = \mathbf{k}_{ph} + \mathbf{k}_0$. There are now two summations to account for two field inversions.

To analyze effects of the terms in equation (33) we explicitly write the equations for functions $S_{l',l}^{(2)}(\mathbf{k})$:

$$\begin{aligned}
S_{1,1}^{(2)}(\mathbf{k}) &= Q_{1,1}^{(+)} Q_{1,1}^{(-)} e^{i\varphi_0} \int e^{i\left(\mathbf{k}_{ph} + (\mathbf{k}_r - \mathbf{k}_0)\right)\cdot\mathbf{r}} e^{i\theta_{1,1}(\mathbf{r})} I(\mathbf{r}) d^3r\,, \\
S_{1,0}^{(2)}(\mathbf{k}) &= Q_{1,1}^{(+)} Q_{1,0}^{(-)} \int e^{i(\mathbf{k}_r - 2\mathbf{k}_0)\cdot\mathbf{r}} e^{i\theta_{1,0}(\mathbf{r})} I_r(\mathbf{r}) d^3r\,, \\
S_{1,-1}^{(2)}(\mathbf{k}) &= Q_{1,1}^{(+)} Q_{1,-1}^{(-)} e^{-i\varphi_0} \int e^{i\left(-\mathbf{k}_{ph} + (\mathbf{k}_r - 3\mathbf{k}_0)\right)\cdot\mathbf{r}} e^{i\theta_{1,-1}(\mathbf{r})} I(\mathbf{r}) d^3r\,, \\
S_{-1,1}^{(2)}(\mathbf{k}) &= Q_{1,-1}^{(+)} Q_{-1,1}^{(-)} e^{i\varphi_0} \int e^{i\left(\mathbf{k}_{ph} + (\mathbf{k}_r + 3\mathbf{k}_0)\right)\cdot\mathbf{r}} e^{i\theta_{1,1}(\mathbf{r})} I(\mathbf{r}) d^3r\,, \\
S_{-1,0}^{(2)}(\mathbf{k}) &= Q_{1,-1}^{(+)} Q_{-1,0}^{(-)} \int e^{i(\mathbf{k}_r + 2\mathbf{k}_0)\cdot\mathbf{r}} e^{i\theta_{1,0}(\mathbf{r})} I_r(\mathbf{r}) d^3r\,, \\
S_{-1,-1}^{(2)}(\mathbf{k}) &= Q_{1,-1}^{(+)} Q_{-1,-1}^{(-)} e^{-i\varphi_0} \int e^{i\left(-\mathbf{k}_{ph} + (\mathbf{k}_r + \mathbf{k}_0)\right)\cdot\mathbf{r}} e^{i\theta_{1,-1}(\mathbf{r})} I(\mathbf{r}) d^3r\,, \\
S_{0,1}^{(2)}(\mathbf{k}) &= Q_{1,0}^{(+)} Q_{0,1}^{(-)} e^{i\varphi_0} \int e^{i\left(\mathbf{k}_{ph} + (\mathbf{k}_r + \mathbf{k}_0)\right)\cdot\mathbf{r}} e^{i\theta_{1,1}(\mathbf{r})} I(\mathbf{r}) d^3r\,, \\
S_{0,0}^{(2)}(\mathbf{k}) &= Q_{1,0}^{(+)} Q_{0,0}^{(-)} \int e^{i\mathbf{k}_r\cdot\mathbf{r}} e^{i\theta_{1,0}(\mathbf{r})} I_r(\mathbf{r}) d^3r\,, \\
S_{0,-1}^{(2)}(\mathbf{k}) &= Q_{1,0}^{(+)} Q_{0,-1}^{(-)} e^{-i\varphi_0} \int e^{i\left(-\mathbf{k}_{ph} + (\mathbf{k}_r - \mathbf{k}_0)\right)\cdot\mathbf{r}} e^{i\theta_{1,-1}(\mathbf{r})} I(\mathbf{r}) d^3r.
\end{aligned} \tag{34}$$

The trajectories of the selected $S_{l',l}^{(2)}(\mathbf{k})$ having the greatest impact on the reconstructed image are shown in Fig. 3.

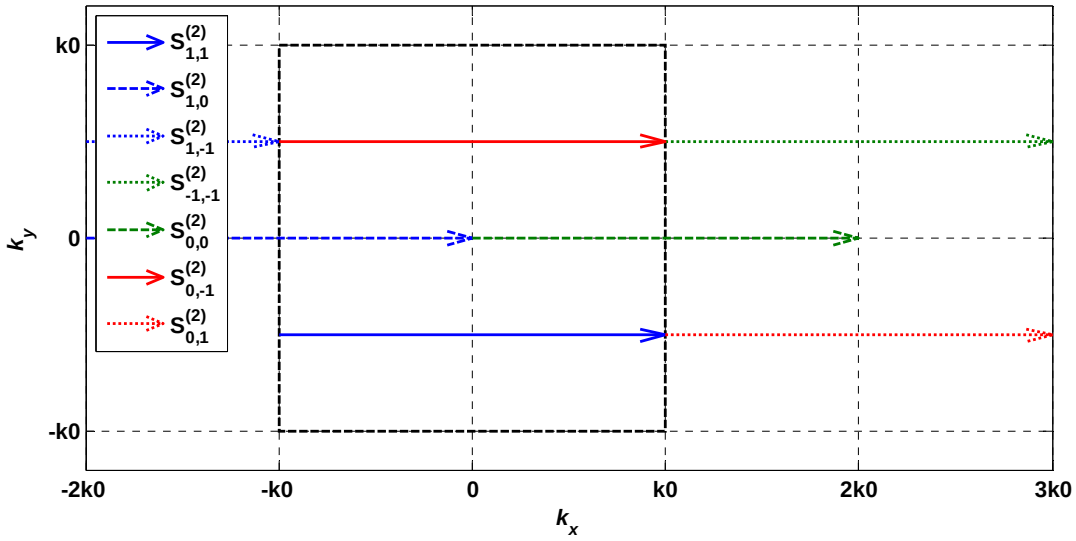

Fig. 3. *K*-space trajectories for the second echo. The dashed rectangle denotes the sampled area. The term $\boldsymbol{S^{(2)}_{1,1}}$ describes the trajectory in the case of ideal non-adiabatic field inversion. All other terms arise in the case of non-ideal field inversion.

From equations (34) and Fig. 3 we can see that the term $S^{(2)}_{1,1}(\mathbf{k})$ corresponds to the main image from the second echo. Note that during the second echo the phase encoding directions are flipped relative to the first echo (compare $S^{(1)}_{-1}(\mathbf{k})$ and $S^{(2)}_{1,1}(\mathbf{k})$).

The term $S^{(2)}_{0,-1}(\mathbf{k})$, as is evident from Fig. 3, forms an echo signal that produces a "ghost" artifact that is flipped about the phase encoding direction, relative to the main image, with different phase and amplitude. Taking into account that $S^{(2)}_{0,-1}(\mathbf{k})$ is proportional to $Q^{(-)}_{0,-1}$, the physical meaning of this term becomes clear: this signal is caused by the component of magnetization aligned with the measurement field after the first field inversion (step 2 of the pulse sequence, see equation (16)), due to non-ideality of the inversion. During the first echo readout this magnetization vector, being aligned with the magnetic field, stays constant and does not contribute to the MRI signal. However, it comes into play again after the next non-ideal field inversion, resulting in an echo signal during the second echo readout.

The terms $S^{(2)}_{1,0}(\mathbf{k})$ and $S^{(2)}_{0,0}(\mathbf{k})$ form FID like signals, respectively, coming into phase and coming out of phase, resulting in the line artifact similar to that due to $S^{(1)}_{0}(\mathbf{k})$. The remaining terms, i.e. $S^{(2)}_{1,-1}(\mathbf{k})$, $S^{(2)}_{-1,-1}(\mathbf{k})$, $S^{(2)}_{0,1}(\mathbf{k})$, etc., result in vanishing artifacts similar to the artifact caused by the term $S^{(1)}_{1}(\mathbf{k})$ (i.e. at high frequencies).

Repeating these combinatory exercises, *i.e.*, constructing terms proportional to $Q^{(\pm)}_{\pm 1,l'''} \ldots Q^{(+)}_{l'',l'} Q^{(-)}_{l',l}$, one can derive formulae for the detected MRI signal during any subsequent echo interval. We note that in the case of adiabatic field inversion the same analysis applies and similar artefacts will appear due to inability to achieve a true adiabatic field rotation.

F. Numerical Examples

To estimate the magnitude of the $Q_{l',l}^{(\pm)}$ coefficients we will consider two special cases of a non-ideal non-adiabatic field inversion, i.e. the intermediate case, where $|\omega(t)| < |\psi(t)|$, but the term $\omega\hat{\mathbf{b}}_0^{\times}$ cannot be neglected in equation (7).

In the first case, we assume that the direction of the effective magnetic field in the rotating frame of reference is constant. This stat condition means that the magnetic field is rotated around a static axis $\hat{\mathbf{u}} = \cos(\alpha)\,\hat{\mathbf{e}}_x + \sin(\alpha)\,\hat{\mathbf{e}}_y$ in such manner that $\omega(t)/\psi(t) = a/b = const$, where a and b are constants such that $a^2 + b^2 = 1$. In this case the matrix $\mathbf{U}_{\pm}$, being the solution of equation (7) with $\mathbf{\Omega}_{eff}^{\times} = \omega_{eff}(t)(\pm a\hat{\mathbf{e}}_z^{\times} + b\hat{\mathbf{u}}^{\times})$, is equal to:

$$\mathbf{U}_{\pm} = e^{-\varphi_{eff}\hat{\mathbf{b}}_{eff}^{\times}}, \tag{35}$$

where $\hat{\mathbf{b}}_{eff}^{\times} = \pm a\hat{\mathbf{e}}_z^{\times} + b\hat{\mathbf{u}}^{\times}$, $\varphi_{eff} = \int_0^{T_{inv}} \omega_{eff}(t')dt'$, and $\omega_{eff}(t) = \sqrt{\omega^2(t) + \psi^2(t)}$.

Expanding the matrix $e^{\pi\hat{\mathbf{u}}^{\times}} \cdot \mathbf{U}_{\pm}$ in a Taylor series assuming $|\omega(t)| < |\psi(t)|$, and keeping only terms to the second order of a/b, we obtain the following expression for the coefficients $Q_{l',l}^{(\pm)}$, which we will write in matrix notation:

$$\begin{aligned}\mathbf{Q}^{(\pm)} \equiv \left[Q_{l',l}^{(\pm)}\right] = \begin{bmatrix}1 & 0 & 0\\ 0 & 1 & 0\\ 0 & 0 & 1\end{bmatrix} \pm \sqrt{2}\varepsilon \begin{bmatrix}0 & e^{-i\alpha} & 0\\ -e^{i\alpha} & 0 & -e^{-i\alpha}\\ 0 & e^{i\alpha} & 0\end{bmatrix} + \\ +\varepsilon^2 \begin{bmatrix}-1 & -\frac{i\pi}{2\sqrt{2}}e^{-i\alpha} & -e^{-i2\alpha}\\ -\frac{i\pi}{2\sqrt{2}}e^{i\alpha} & -2 & \frac{i\pi}{2\sqrt{2}}e^{-i\alpha}\\ -e^{i2\alpha} & \frac{i\pi}{2\sqrt{2}}e^{i\alpha} & -1\end{bmatrix} + O(\varepsilon^3).\end{aligned} \tag{36}$$

Here $\varepsilon = a/b$, the first index enumerates rows of the matrix and the second index enumerates columns. From equation (36) it follows that for the first echo the amplitude of the artifact free image is proportional to $(1 - 2\varepsilon^2)$, while the amplitude of the line artifact is proportional to ε. During the second echo the amplitude of the primary image corresponding to the term $S_{1,1}^{(2)}(\mathbf{k})$ in equation (34) is proportional to $(1 - 2\varepsilon^2)^2$, while amplitude of the "ghost" artifact corresponding to the term $S_{0,-1}^{(2)}(\mathbf{k})$ is proportional to ε^2, and amplitude of the line artifacts from terms $S_{1,0}^{(2)}(\mathbf{k})$ and $S_{-1,-1}^{(2)}(\mathbf{k})$ is proportional to ε and ε^2, respectively.

As a second example we assume that the magnetic field is rotated around a static axis $\hat{\mathbf{u}}$ defined previously in such manner that rotation from 0 to angle ε happens adiabatically, then from angle ε to angle $\pi - \varepsilon$ the rotation is non-adiabatic, and, finally, rotation from angle $\pi - \varepsilon$ to π is again adiabatic. This case describes inversion of a field in the presence of a smaller constant orthogonal field. In this case we can write the matrix $e^{\pi\hat{\mathbf{u}}^{\times}} \cdot \mathbf{U}_{\pm}$ as a combination of the following rotations:

$$e^{\pi\hat{\mathbf{u}}^{\times}} \cdot \mathbf{U}_{\pm} = e^{\pi\hat{\mathbf{u}}^{\times}} \cdot e^{\pm\vartheta_{\varepsilon}\hat{\mathbf{e}}_z^{\times}} \cdot e^{-(\pi-2\varepsilon)\hat{\mathbf{u}}^{\times}} \cdot e^{\pm\vartheta_{\varepsilon}\hat{\mathbf{e}}_z^{\times}}, \tag{37}$$

where the phase angle $\vartheta_{\varepsilon} = \int_0^{T_{\varepsilon}} \omega(t')dt'$, and T_{ε} is defined by the condition $\varepsilon = \int_0^{T_{\varepsilon}} \psi(t')dt'$.

Equation (37) may be evaluated explicitly to compute the coefficients $Q_{l',l}^{(\pm)}$ according to equation (23):

$$\mathbf{Q}^{(\pm)} = \begin{bmatrix} \cos^2(\varepsilon) & -\frac{i}{\sqrt{2}}\sin(2\varepsilon)e^{i\Phi_{\pm}} & \sin^2(\varepsilon)e^{i2\Phi_{\pm}} \\ -\frac{i}{\sqrt{2}}\sin(2\varepsilon)e^{-i\Phi_{\pm}} & \cos(2\varepsilon) & \frac{i}{\sqrt{2}}\sin(2\varepsilon)e^{i\Phi_{\pm}} \\ \sin^2(\varepsilon)e^{-i2\Phi_{\pm}} & \frac{i}{\sqrt{2}}\sin(2\varepsilon)e^{-i\Phi_{\pm}} & \cos^2(\varepsilon) \end{bmatrix}, \tag{38}$$

where $\Phi_{\pm} = \pm\vartheta_{\varepsilon} - \alpha$. Expanding equation (38) in a Taylor series and keeping only terms up to the second order of ε we obtain the following equation:

$$\begin{aligned} \mathbf{Q}^{(\pm)} = &\begin{bmatrix} 1 & 0 & 0 \\ 0 & 1 & 0 \\ 0 & 0 & 1 \end{bmatrix} + \sqrt{2}\varepsilon \begin{bmatrix} 0 & -ie^{i\Phi_{\pm}} & 0 \\ -ie^{-i\Phi_{\pm}} & 0 & ie^{i\Phi_{\pm}} \\ 0 & ie^{-i\Phi_{\pm}} & 0 \end{bmatrix} + \\ &+\varepsilon^2 \begin{bmatrix} -1 & 0 & e^{i2\Phi_{\pm}} \\ 0 & -2 & 0 \\ e^{-i2\Phi_{\pm}} & 0 & -1 \end{bmatrix} + O(\varepsilon^3). \end{aligned} \tag{39}$$

This last expression is very similar to equation (36), and again the terms $Q_{0,\pm1}^{(\pm)}$ and $Q_{\pm1,0}^{(\pm)}$ are proportional to ε, diagonal terms $Q_{l,l}^{(\pm)}$ are proportional to $(1-2\varepsilon^2)$, and anti-diagonal terms $Q_{\pm1,\mp1}^{(\pm)}$ are proportional to ε^2.

Fig. 4 illustrates these effects in a general case using numerical simulation.

a) Non-adiabatic:

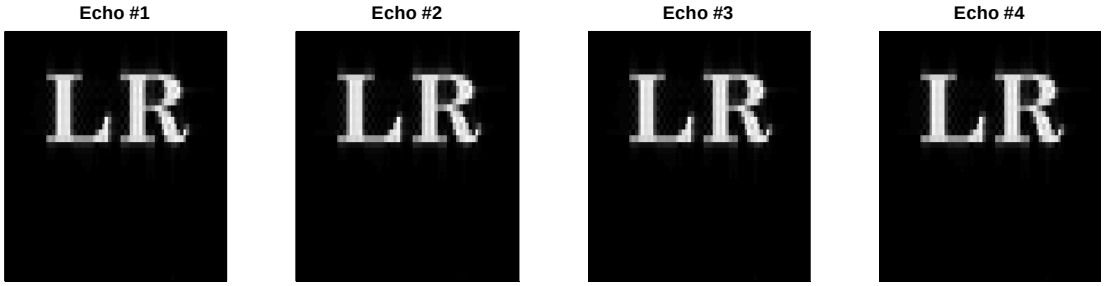

b) Adiabatic:

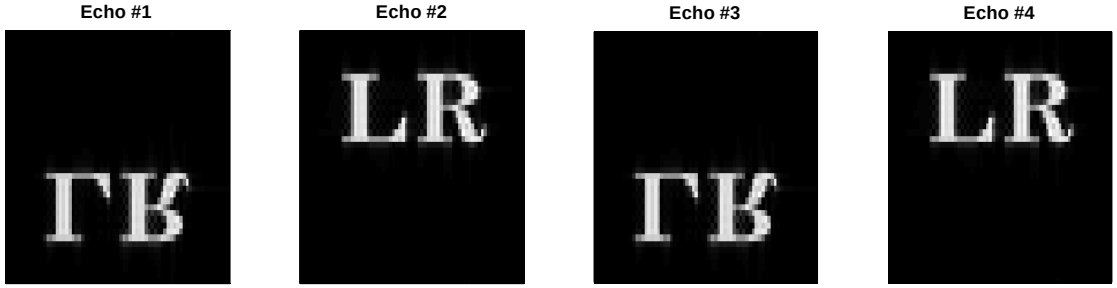

c) Intermediate:

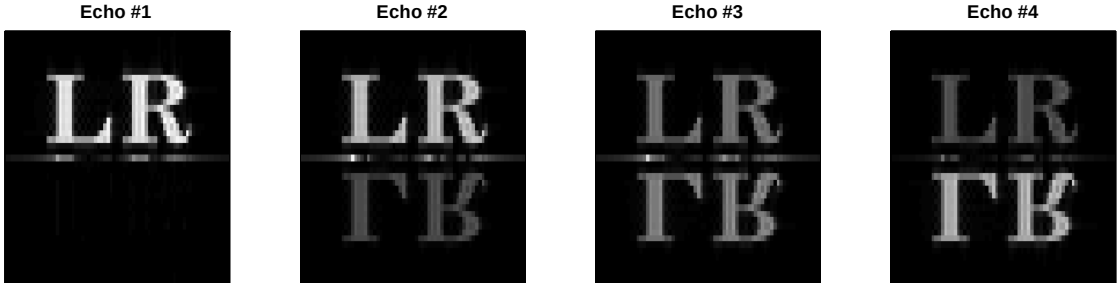

d) Intermediate, $m_z(\mathbf{r})$ is set to 0 at the beginning of the first echo readout.

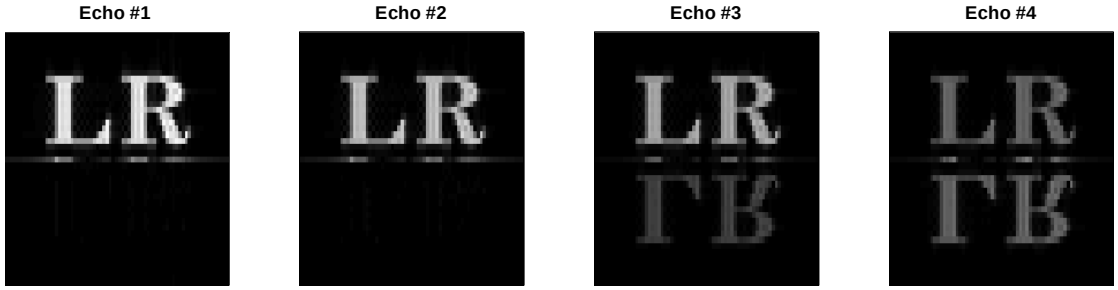

Fig. 4. Numeric simulation of adiabatic vs. non-adiabatic transition. The horizontal coordinate corresponds to the frequency encoded direction, and the vertical coordinate represents the phase encoded direction, which is flipped for the second and fourth echo.

The top row in

Fig. 4 shows four reconstructed echo images (using the pulse sequence in Fig. 1) wherein the direction of the magnetic field was flipped in the ideal non-adiabatic condition. The second row represents the ideal adiabatic condition, and we see that object position at odd numbered echoes

is flipped about the readout axis. The flipping is due to the $e^{i(\mathbf{k}_{rd}-\mathbf{k}_{ph})\cdot\mathbf{r}}$ term in (29), as compared to the $e^{i(\mathbf{k}_{rd}+\mathbf{k}_{ph})\cdot\mathbf{r}}$ term in (31).

The third row of

Fig. 4 illustrates the intermediate case, wherein the presence of both terms, i.e. $e^{i(\mathbf{k}_{rd}-\mathbf{k}_{ph})\cdot\mathbf{r}}$ and $e^{i(\mathbf{k}_{rd}+\mathbf{k}_{ph})\cdot\mathbf{r}}$, results in ghost artifacts for which the amplitude increases in each successive echo. Here it is assumed that 10% of the magnetization was initially aligned with the measurement field, resulting in the line artifact apparent in the figure.

The fourth row illustrates the case wherein the residual magnetization along the *z*-axis is intentionally set to zero after the first field inversion, i.e. at the beginning of the first echo readout. In this case the "ghost" artifact in the second echo is removed.

III. EXPERIMENTS

To illustrate how these ghost artifacts can appear in a real imaging system, we show results from a ULF-MRI machine constructed for the detection of liquid explosives [20]. Due to space constraints, the magnetic shield for this system was far closer to the sample volume than in most of our other systems. The pulse sequence shown in Fig. 1 was used, but the actual field switching falls into the intermediate case at a Larmor frequency of ~3 kHz. Fig. 5 shows the *x*-*y*-*z* components of the B_m field during a pulse sequence as measured by a fluxgate at the iso-center of the system. The elliptical nature of the vector path is due to transient fields induced by switching the polarity of the measurement field B_m, and illustrates rotation of the magnetic field during the switching. The magnitude of the measurement field B_m is about 90 μT, and the magnitude of the transient fields orthogonal to B_m is about 3 μT.

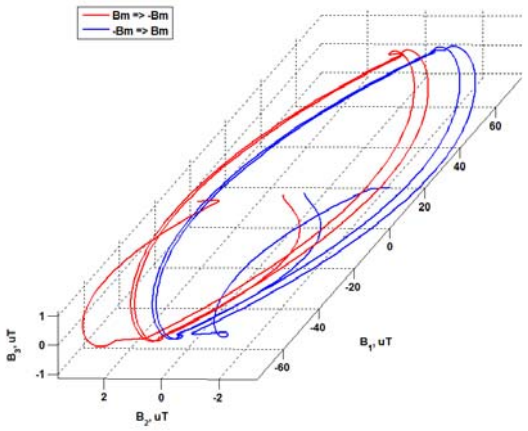

Fig. 5. Measurement field inversion in one experimental ULF-MRI system: 3D representation of magnetic field vector trajectory during the transition from one polarity to the other.

Illustrative echo images from the device are shown in Fig. **6.** To obtain the images presented here we used a two dimensional gradient echo sequence. Four echoes were acquired. Parameters of the imaging sequence are summarized in Table 1.

Table 1. Parameters of the imaging sequence

Polarization time, T_p	3000 ms
Encoding time, T_e	50 ms
Readout time, T_{acq}	100 ms
Readout gradient, G_x	2.0 Hz/mm
Number of phase encoding steps, N_y	41

Phase encoding gradient range, G_y	±1.4 Hz/mm
Phase encoding gradient step, ΔG_y	35 mHz/mm
Total imaging time, T_{tot}	231 s

A uniform water phantom consisting of a cylinder ~250 mm in diameter and 75 mm deep was placed in the system, and the images shown are for one of the 7 sensors used for full imaging.

The bright spot in the upper left of the images represents the sensitivity of that particular channel to the water phantom, shown clearly and accurately in the first echo. In the middle row we show images from subsequent echoes wherein field switching is as described by the blue trace (top row), that is, not fast enough compared to the residual fields to achieve the ideal non-adiabatic condition. In the bottom row we show images after faster field switching was implemented (top row, green trace). The ghost artifact in the middle row for the second and following echoes appears with increasing amplitude in each subsequent echo due to the effects described above. Although it might appear much like an aliasing artifact, this phenomenon is in fact the result of failure to attain a true non-adiabatic inversion of the measurement field.

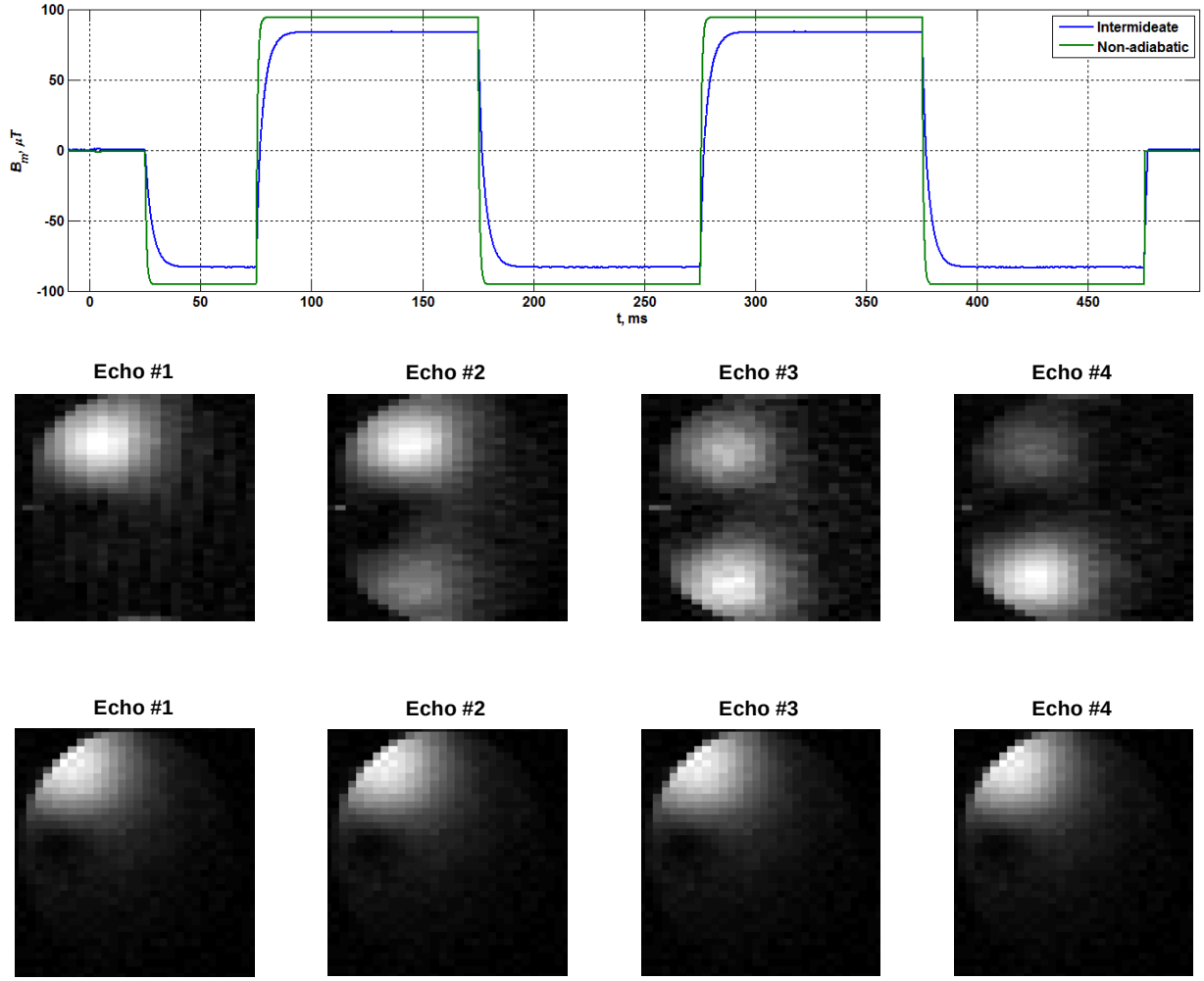

Fig. 6. Top row: measurement field inversion recordings, middle row: echo images for "slow" (blue trace) field inversion, bottom row: echo images for "fast" (green trace) field inversion.

IV. DISCUSSION & CONCLUSIONS

The pursuit of MRI at ULF by our group and others has necessitated a reexamination of the influence of transient magnetic fields produced in nearby conducting materials. In particular, these effects can become quite pronounced at ULF because the method relies on pulsed pre-polarization in the vicinity of conductive magnetic shields (mu-metal and/or aluminum), and the measurement and gradient fields themselves are low enough to be comparable to the transient fields produced. One of the effects of transient fields associated with the inversion of the measurement field during a multiple gradient echoe imaging sequence is that a true non-adiabatic field inversion cannot be achieved. In this paper we have introduced a general theoretical framework describing the origin of a "ghost" artifact associated with failure to achieve a true non-adiabatic inversion of the measurement field. We have shown that this model can accurately explain the artifacts observed in a ULF MRI system during a multiple echo imaging sequence.

While better design of pre-polarization fields [21] and shielding [22] can mitigate these effects, here we present a framework that can explain and provide a foundation for correction of these artifacts.

ACKNOWLEDGEMENTS

Authors gratefully acknowledge DOE, DHS support of this work under the projects LDRD 20130121DR and HSHQPM12X00166.

REFERENCES

[1] J. Clarke, M. Hatridge and M. Mößle, "SQUID-detected magnetic resonance in microtesla fields," *Annual Review of Biomedical Engineering,* **9**, 389-413 (2007).

[2] M. Espy, A. Matlashov and P. Volegov, "SQUID-detected ultra-low field MRI," *Journal of Magnetic Resonance,* **229**, 1-15 (2013).

[3] M. Mößle, S.-I. Han, W. R. Myers, S.-K. Lee, N. Kelso, M. Hatridge, A. Pines and J. Clarke, "SQUID-detected microtesla MRI in the presence of metal," *Journal of Magnetic Resonance,* **179**, 146-151 (2006).

[4] S. K. Lee, M. Mößle, W. Myers, N. Kelso, A. H. Trabesinger, A. Pines and J. Clarke, "SQUID-detected MRI at 132 μT with T1-weighted contrast established at 10 μT-300 mT," *Magnetic Resonance in Medicine,* **53**, 9-14 (2005).

[5] S. Busch, M. Hatridge, M. Mößle, W. Myers, T. Wong, M. Muck, K. Chew, K. Kuchinsky, J. Simko and J. Clarke, "Measurements of T1-Relaxation in *ex vivo* prostate tissue at 132 μT," *Magnetic Resonance in Medicine*, **67**, p. 1138–1145, 2012.

[6] H. W. Fischer, P. A. Rinck, Y. Van Haverbeke and R. N. Muller, "Nuclear relaxation of human brain gray and white matter: Analysis of field dependence and implications for MRI," *Magnetic Resonance in Medicine,* **16**, 317-334 (1990).

[7] P. L. Volegov, A. N. Matlachov, M. A. Espy, J. S. George and R. H. Kraus Jr., "Simultaneous magnetoencephalography and SQUID detected nuclear MR in microtesla magnetic fields," *Magnetic Resonance in Medicine,* **52**, no. 3, 467-470 (2004).

[8] V. S. Zotev, A. N. Matlashov, P. L. Volegov, I. M. Savukov, M. A. Espy, J. C. Mosher, J. J. Gomez and R. H. Kraus Jr., "Microtesla MRI of the human brain combined with MEG," *Journal of Magnetic Resonance,* **194**, 115-120 (2008).

[9] P. E. Magnelind, J. J. Gomez, A. N. Matlashov, T. Owens, J. H. Sandin, P. L. Volegov and M. A. Espy, "Co-registration of interleaved MEG and ULF MRI using a 7 Channel low-T_c SQUID system," *IEEE Transactions on Applied Superconductivity,* **21**, 456–460 (2011).

[10] P. T. Vesanen, J. O. Nieminen, K. C. J. Zevenhoven, J. Dabek, L. T. Parkkonen, A. V. Zhdanov, J. Luomahaara, J. Hassel, J. Penttilä, J. Simola, A. I. Ahonen, J. P. Mäkelä and R. J. Ilmoniemi, "Hybrid ultra-low-field MRI and magnetoencephalography system based on a commercial whole-head neuromagnetometer," *Magnetic Resonance in Medicine,* **69**, 1795-1804 (2013).

[11] Y.-C. Hsu, P. T. Vesanen, J. O. Nieminen, K. C. J. Zevenhoven, J. Dabek, L. Parkkonen, I.-C. Chern, R. J. Ilmoniemi and F. S. Lin, "Efficient concomitant and remanence field artifact reduction in ultra-low-field MRI using a frequency-space formulation," *Magnetic Resonance in Medicine*, **71**, 955-965 (2014).

[12] A. Abragam, *Principles of Nuclear Magnetism*, Oxford, 1961.

[13] E. T. Jaynes, "Matrix treatment of nuclear induction," *Physical Review*, **98**, no. 4, 1099-1105 (1955).

[14] W. Kahan, "Notes for math. H110, computing cross-products and rotations in 2- and 3-dimensional Euclidean spaces," 2 3 2008. [Online]. Available: http://www.cs.berkeley.edu/~wkahan/MathH110/Cross.pdf . [Accessed 30 10 2012].

[15] G. A. Korn and T. M. Korn, *Mathematical Handbook for Scientists and Engineers*, New York: Dover Publications Inc., 2000.

[16] F. R. Gantmacher, *The Theory of Matrices*, AMS Chelsea Publishing, 2000.

[17] P. L. Volegov, J. C. Mosher, M. A. Espy and R. Kraus, "On concomitant gradients in low-field MRI," *Journal of Magnetic Resonance*, **175**, 103-113 (2005).

[18] J. O. Nieminen and R. J. Ilmoniemi, "Solving the problem of concomitant gradients in ultra-low-field MRI," *Journal of Magnetic Resonance*, **207**, 213-219 (2010).

[19] P. Callaghan, *Principles of Nuclear Magnetic Resonance Microscopy*, Oxford, 2004.

[20] M. Espy, M. Flynn, J. Gomez, C. Hanson, R. Kraus, P. Magnelind, K. Maskaly, A. Matlashov, S. Newman, T. Owens, M. Peters, H. Sandin, I. Savukov, L. Schultz, A. Urbaitis, P. Volegov and V. Zotev, "Ultra-low-field MRI for the detection of liquid explosives," *Superconductor Science and Technology*, **23**,1-8 (2010).

[21] J. O. Nieminen, P. T. Vesanen, K. C. J. Zevenhoven, J. Dabek, J. Hassel, J. Luomahaara, J. S. Penttila and R. J. Ilmoniemi, "Avoiding eddy-current problems in ultra-low-field MRI with self-shielded polarizing coils," *Journal of Magnetic Resonance*, **212**, 154-160 (2011).

[22] K. Zevenhoven, "Solving transient problems in ultra-low-field MRI (Master's thesis)," Aalto University, Helsinki, 2011.